3-D Elastic Time-Reverse Imaging of a Linear Void Anomaly

This paper is a non-peer reviewed preprint submitted to EarthArXiv
The paper has been submitted for peer review to Geophysics

Madeleine Pels
Department of Geophysics
Colorado School of Mines
Golden, Co 80401
MadeleinePels1225@gmail.com

Jeffrey Shragge
Department of Geophysics
Colorado School of Mines
Golden, Co 80401

Aaron J. Girard
Department of Geophysics
Colorado School of Mines
Golden, Co 80401

ABSTRACT

Imaging meter-scale subsurface heterogeneities such as void spaces remains a difficult task for most established near-surface seismic methods. One strategy for addressing this challenge is to isolate and use surface waves backscattered from lateral heterogeneities to identify and characterize the sources of scattered energy. Seismic methods associated with this strategy, though, often require dense geophone sampling, demand significant user-intensive preprocessing, and/or involve large computation run times. These limitations motivate the development of more effective and efficient near-surface seismic analysis approaches. One way to address such challenges is to use elastic time reverse imaging (E-TRI), a migration method originally proposed for microseismic event location. E-TRI propagates two wavefields in reverse time and then applies an imaging condition to generate an image of the source locations of scattered energy. When adapted for detecting near-surface heterogeneities, the two wavefields are the estimated outward-propagating transmission and inward-propagating scattered surface-wave energy. These wavefields are used in an elastic imaging condition that correlates temporally and spatially collocated energy to image the sources of surface-wave scattering. Synthetic tests demonstrate the ability of E-TRI to image meter-scale heterogeneities at seismic wavelengths between 2.0-5.0$\times$ the characteristic scale length of the introduced subsurface anomalies. Results from a field test using 3-D seismic data acquired at the Yuma Proving Grounds highlight E-TRI's ability to detect a purpose-built long linear void space of meter-scale cross-sectional area located at 10 m depth. The results suggest that E-TRI, perhaps with improved depth sensitivity through more advanced imaging conditions, would be a reliable near-surface seismic method for characterizing small-scale heterogeneity in complex geological environments.

Keywords Seismic · Near Surface · Imaging · Active Source · Void

1 Introduction

Strong near-surface lateral heterogeneities, such as subsurface void spaces, can pose a combination of geological and geotechnical challenges to society, particularly in the context of infrastructure deployment and monitoring. For example, karst dissolution phenomena and the associated development of larger cavities can lead to drilling hazards, sinkholes, and damage to existing pipeline infrastructure (Cardarelli et al., 2010; James and Ferreira, 2013; Ivanov et al., 2013) if not detected in a timely fashion or left unchecked. Similarly, abandoned infrastructure with void spaces originating from former mining works can continue to erode and cause similar problems as in karst scenarios (Billington et al., 2006; Cardarelli et al., 2010; Ivanov et al., 2016). Other anthropogenic examples posing safety and security risks include shallow clandestine tunnels dug beneath borders or secure facilities that are used to transport human traffic, contraband or other hazardous cargo (Schwenk et al., 2016; Smith et al., 2019). The geophysical targets associated with detecting these void spaces commonly represent meter-scale near-surface anomalies embedded at depths of meters to a few tens of meters, often with lateral extents of hundreds of meters. The dimensions of these smaller-scale voids present detectability difficulties for noninvasive surface-based observation, which motivates the development of new geophysical subsurface characterization techniques capable of addressing these challenges.

Numerous geophysical void detection strategies have been proposed over the past few decades. For example, James and Ferreira (2013) highlight various targeted void-detection survey techniques, including ground penetrating radar (Xu et al., 2010), (micro)gravity (Rybakov et al., 2001; Styles et al., 2006), and various electrical (Rodríguez Castillo and Reyes Gutiérrez, 1992) or magnetic and electromagnetic (Rybakov et al., 2005; Mochales et al., 2007) methods. Most of these methods require dense sampling, often in hard to access or restricted areas where voids are suspected to be located, and do not necessarily lend themselves to larger-scale detection surveys. Similarly, the depth of investigation floors for many existing methods are shallower than 10 m, which presents a challenge as many potential void targets are deeper and such analyses could lead to false negative findings.

Seismic methods have long been used to detect small-scale lateral heterogeneities in multiple fields (Levander and Holliger, 1992). Within near-surface seismic applications, early approaches used P-wave reflections and refractions at frequencies exceeding 100 Hz (Ballard et al., 1982; Miller and Steeples, 1991). However, detecting small anomalies using P-wave data at typical sub-100 Hz near-surface seismic source frequencies is challenging, as seismic wavelengths (λ) on the order of tens of meters are generally much longer than the characteristic meter-scale length of the anomalies to be detected, and thus fall below the detectability threshold (i.e., herein assumed to fall between 0.10-0.25λ depending on the data signal-to-noise level). Other seismic methods for detecting near-surface heterogeneities use scattered SH-wave (Peterie and Miller, 2015) or surface-wave (Sloan et al., 2015) energy, both of which exploit the shorter seismic wavelengths of these wave types compared to P waves and have yielded promising meter-scale heterogeneity detection results.

One way to evaluate the applicability of different seismic methods for such detection challenges is to demonstrate their capabilities on a common data set acquired at a well-characterized survey site. One such site is the Yuma Proving Ground (YPG) in Arizona, United States, which has been the focus of multiple seismic void detection and imaging feasibility studies and has proven to be a valuable testbed for comparing seismic void detection techniques (Sloan et al., 2015; Morton et al., 2017). Chosen for its isolated location away from anthropogenic noise sources (Smith et al., 2019), the YPG site has a well-characterized near-surface elastic velocity structure (Miller et al., 2003) into which a long, linear subsurface void was dug for geophysical testing purposes. To explore the detectability of this void structure, numerous high-density 2-D and one 3-D seismic arrays were deployed over a section of the void space, with active-source multicomponent data sets acquired using an accelerated weight drop as the energy source (Morton et al., 2016).

During the past decade, several near-surface seismic approaches have been tested for void detection using YPG 3-D seismic data sets. Sloan et al. (2015) present a body-wave diffraction study and compare the results with those from backscattered surface-wave techniques. Other studies show the feasibility of processing separated surface-wave energy using multichannel analysis of surface waves (MASW) with shear-wave quality factor (Qs) inversion (Morton et al., 2016) or backscatter analysis of surface waves (BASW) (Schwenk et al., 2016). Peterie et al. (2020) and Peterie et al. (2021) respectively use horizontal-component geophone data for SH- and converted surface-wave diffraction imaging. Full waveform inversion (FWI) has also been applied to the YPG 3-D seismic data set, with the results offering the most accurate constraints on void space locations (Borisov et al., 2017; Smith et al., 2019; Wang et al., 2019). While the aforementioned methods characterized the subsurface void space at the YPG field site with varying degrees of success, common challenges resulted from the need for: (1) a high sampling density to generate well-resolved locations (Smith et al., 2019); (2) an ability to handle the often low signal-to-noise ratios (Schwenk et al., 2016); and/or (3) a large high-performance computing (HPC) effort (Smith et al., 2019). These observations motivate the development of subsurface characterization approaches capable of using sparser, noisier seismic observations with reduced preprocessing and computational intensity requirements.

One way to address these issues is to use an elastic time-reverse imaging (E-TRI) framework. TRI methods were originally applied to passive microseismic data to characterize event locations (Gajewski and Tessmer, 2005; Artman et al., 2010; Chambers et al., 2014; Douma and Snieder, 2014; Nakata and Beroza, 2016; Rocha et al., 2016; Witten and Shragge, 2017; Oren and Shragge, 2021). Microseismic TRI approaches take advantage of the self-adjointness of wave equations and the relative ease at separating larger-magnitude microseismic P- and S-wave arrivals in field data. These methods then use separated P- and S-wave data to reconstruct two (adjoint) wavefields that are propagated in reverse time through a smoothed Earth model with the goal of collapsing the microseismic event energy to its nucleation point (Shragge et al., 2024). The time-reversed wavefields are then used in an elastic imaging condition to generate focusing-based estimates of the microseismic event locations and potentially other source characteristics (Artman et al., 2010; Yuan et al., 2020).

Shragge et al. (2024) recently adapted the E-TRI framework to the problem of backscattered surface-wave imaging of active-source seismic data. Analogous to microseismic event location imaging, the goal of applying E-TRI is to collapse observed scattered surface-wave energy back to the heterogeneity generating the scatterer. For applications in near-surface heterogeneity detection using active-source surveys, E-TRI has been modified to use transmitted and scattered surface-wave energy rather than P- and S-wavefield data (Shragge et al., 2024). This approach relies on the separability and largely opposing propagation directions of transmitted and backscattered surface waves, which can be accomplished using time-space $t-x$ muting or Fourier-domain frequency-wavenumber $f-k$ dip-filtering approaches.

The work herein applies the adapted E-TRI framework to the problem of void identification at the YPG field site and compares its efficacy with other reported methods. In particular, we test E-TRI's ability to detect and image meter-scale subsurface void anomalies. We begin with a discussion of the YPG field site geology and the acquired 3-D near-surface seismic data set used for the following field data tests. Next, we summarize the results of near-surface seismic methods applied to date at the YPG field site to provide a detectability baseline. We then review the E-TRI method and examine the feasibility of applying E-TRI for near-surface void detection, including outlining our approaches to preprocessing and partitioning transmitted and backscattered surface-wave energy. We then apply the E-TRI framework to synthetic and field YPG data sets using a 1-D reference elastic model and conduct experiments for synthetic 2-D data sets modeled with 5-35 Hz and 10-50 Hz Ormbsy wavelets, along with tests involving positioning the void anomaly at various model depths between 5.0 m to 15.0 m. Finally, we present the YPG 3-D case history to illustrate the imaging potential of E-TRI for near-surface void detection. The paper concludes with discussions of computational run-time considerations, depth sensitivity of E-TRI analyses, and the general extensibility of the E-TRI method to related detection and imaging challenges.

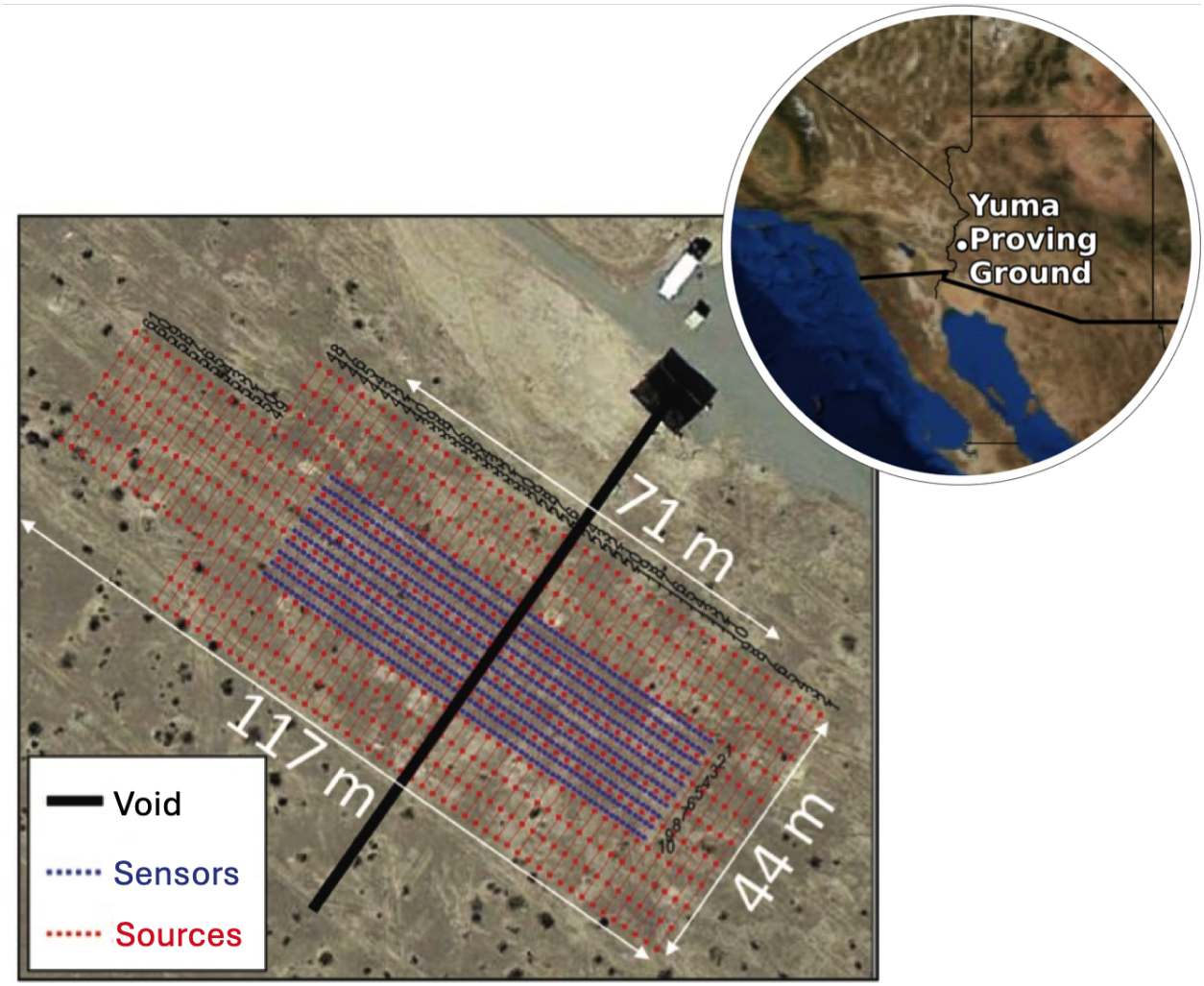

Figure 1: YPG field site with an overlay of seismic acquisition geometry. The red and blue dots respectively represent source and receiver geophone locations. The long, linear void space (indicated by the solid black line) is situated at 10 m depth and passes beneath the center of the geophone array (after Smith et al., 2019). The inset map shows the YPG field site location in western Arizona, USA.

2 Field Site and Previous Analyses

The YPG field site is located in the Sonoran Desert of the Basin and Range Province in southwestern Arizona, United States (see inset map of Figure 1). The site is representative of a flat and arid desert environment, with borehole data indicating that the top 100 m is composed of varying amounts of unconsolidated sand and silt, with clay units found at depth (Miller et al., 2003). The site is characterized by low environmental noise aside from wind and occasional foot traffic (Smith et al., 2019). To develop a physical testbed for geophysical and related field studies, a void of dimensions 0.9 m width, 1.5 m height, and 96 m length was hand dug at an average depth of 10 m (Sloan et al., 2015). Figure 1 shows the orientation of the void transect.

A 3-D multicomponent seismic data set was acquired over a section of the void system using 720 4.5 Hz geophones and an accelerated weight drop source (Morton et al., 2016). Figure 1 illustrates the acquisition geometry defined by ten lines of 72 receiver channels (blue dots) with 1.0 m inline and 2.0 m crossline sampling centered over the void. A total of 12 source lines were acquired at a 2.0 m inline and 4.0 m crossline sampling (red dots), with some source points located off all four sides of the receiver grid, for a total of 654 sources with a maximum of 112 m source-receiver offset. We note that the multicomponent data were not acquired simultaneously on 3-C geophones; rather, single-component

vertical and horizontal (in two orientations) geophones were sequentially deployed with the source grid thrice repeated. Although the present work is restricted to vertical-component geophone data, this does not represent a methodological restriction of E-TRI analyses.

2.1 Previous Field Site Studies

Multichannel analysis of surface waves (MASW) conducted on a 2-D near-surface seismic data set acquired at the YGP site prior to void construction proved to be a robust method to estimate the 1-D V_S profile of the upper 30 m (Ivanov et al., 2005; Rickards et al., 2011). However, MASW analyses are often criticized for low lateral resolution because the approach effectively averages the velocity distributions across the array aperture (Boiero and Socco, 2011). Consequently, the MASW results reported by Morton et al. (2017) using a nine-component 2-D seismic dataset were unable to detect the void anomaly.

To address these concerns, Schwenk et al. (2014) and Schwenk et al. (2016) developed and applied the backscattered analysis of surface waves (BASW) technique. In this method, backscattered energy is first separated from the transmitted wavefield before applying a dynamic linear move-out correction estimated from a dispersion curve. Shot gathers are then sorted into common receiver stacks, which are subsequently processed into the final BASW image. Similarly, Peterie et al. (2021) and Ivanov et al. (2024) develop the converted-surface-wave imaging (CSWI) technique that takes advantage of forward-propagating converted surface waves. Although the computationally efficient BASW method clearly detected the void anomaly not evident in MASW results, the main drawback is the relatively low lateral and vertical resolution of the detected void anomaly, with the CSWI method helping to increase the signal-to-noise ratio (SNR).

Several additional methods tested at the YPG site involved isolating P-S converted diffractions (Peterie and Miller, 2015) or backscattered SH-wave energy (Peterie et al., 2020). Similar to BASW, these processing efforts used $f-k$ filtering to separate the transmitted and backscattered data contributions with minimal wavefield distortion based on opposing wavefield dips. The separated backscattered energy estimates are then stacked to better localize the sources of observed SH-wave diffraction energy. Although the above methods arguably are more straightforward to apply than BASW and effectively constrain the lateral location of the YPG void anomaly to within ± 5.0 m of the true position, the results tend to exaggerate the estimated depth (as estimated by zero-offset two-way travel times calculated through a 1-D V_s model) from 9 m to approximately 12 m due to velocity profile uncertainty and asymmetric travel paths. In addition, Sloan et al. (2015) showed that the joint interpretation of body-wave diffraction and BASW results improves the confidence in co-located void estimates as these methods leverage complementary wavefield components.

Finally, Borisov et al. (2017) and Smith et al. (2019) applied 3-D E-FWI to the YPG seismic data set, with the results offering the most accurate void characterization. However, a drawback of the reported E-FWI approach is that it required both dense seismic acquisition and an associated significant computational effort (i.e., one million CPU hours on an HPC cluster system). Recent work by Borisov et al. (2025), though, demonstrates that applying deep learning methods to generate initial source wavelet estimates offers the potential for improved FWI convergence and inversion result accuracy.

2.2 1-D Reference Model

To test the 3-D E-TRI method for void detection purposes, we developed an isotropic 1-D elastic background model by adapting the results from various previous YPG field site studies. Figure 2 presents the elastic model components $[V_P, V_S, \rho]$ derived from travel-time tomography, surface-wave analysis (Schwenk, 2013) and *a priori* density information (Morton et al., 2016), respectively. The initial smoothed models on which we have based our analyses were constructed using previous site characterization efforts (Borisov et al., 2017). The velocities of the estimated ten-layer Earth model generally increase with depth, though velocity inversions are found between depths of 5-10 m and 20-30 m. Finally, while the isotropic elastic model assumption is generally valid for scenarios involving shallow, poorly unconsolidated sediments like those at the YPG field site, E-TRI can generalize to anisotropic models if required by the geological setting.

3 E-TRI Overview

The E-TRI method relies on considering the observed active-source wavefield u_i as the linear combination of outward-propagating transmission $\tilde{u_i}$ and inward-propagating backscattered δu_i wavefield components such that

$$u_i(\mathbf{s}, \mathbf{x}, t) = \tilde{u_i}(\mathbf{s}, \mathbf{x}, t) + \delta u_i(\mathbf{s}, \mathbf{x}, t), \tag{1}$$

where $\mathbf{s} = (s_x, s_y, 0)$ are the surface source coordinates, $\mathbf{x} = (x, y, z)$ represents the simulation domain, t is time, and a subscript i indicates the vector component. The multicomponent data vector, defined as $d_i = d_i(\mathbf{s}, \mathbf{r}, t) \equiv$

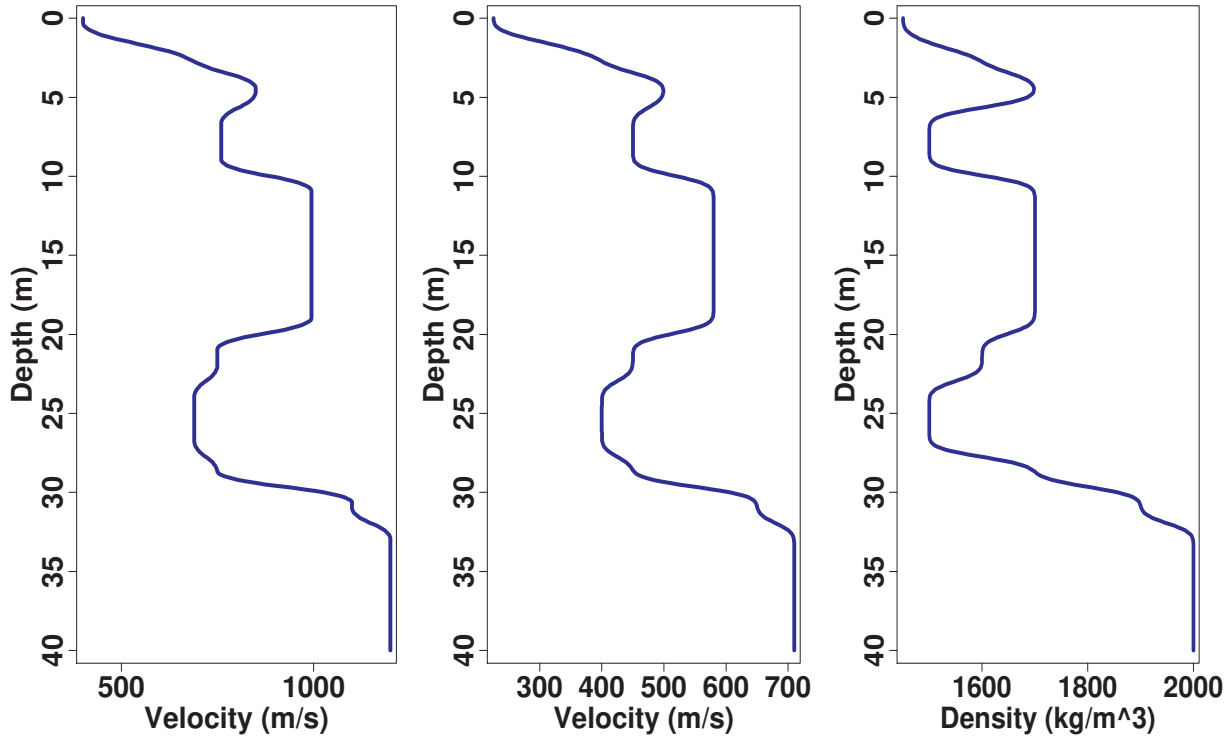

Figure 2: Smoothed 1-D (a) V_P, (b) V_S, and (c) ρ elastic property model estimates adapted from a previous E-FWI study (Borisov et al., 2017).

$u_i|_{(x,y,z)=(r_x,r_y,0)}$ where $\mathbf{r} = (r_x, r_y, 0)$ are the surface receiver locations, can be partitioned into transmission and scattered data components, $\tilde{d}_i$ and δd_i, by applying appropriate signal processing techniques. For example, one can use $t - x$ domain muting (Shragge et al., 2024), $f - k$ dip filtering (Peterie et al., 2020), or by specify more tailored surgical mute operators (Schwenk et al., 2016) to perform wave separation. The union of the two partitioned data sets recovers the observed data vector,

$$d_i(\mathbf{s}, \mathbf{r}, t) = \tilde{d}_i(\mathbf{s}, \mathbf{r}, t) + \delta d_i(\mathbf{s}, \mathbf{r}, t). \tag{2}$$

Conceptually, the transmission wavefield and data, $\tilde{u}_i$ and $\tilde{d}_i$, can be associated with a background 1-D elastic model $\tilde{c}_{ijkl}$. Similarly, the scattered wavefield and data, $\tilde{u}_i$ and $\tilde{d}_i$, are linked to shorter-wavelength heterogeneity Δc_{ijkl} that combine to form the true 3-D elastic Earth model c_{ijkl},

$$c_{ijkl}(\mathbf{x}) = \tilde{c}_{ijkl}(\mathbf{x}) + \Delta c_{ijkl}(\mathbf{x}). \tag{3}$$

TRI analysis commonly applies an imaging condition involving two time-reversed wavefields to image the subsurface locations of "data events". When using transmitted and backscattered surface-wave data, $\tilde{d}_i$ and δd_i, in the E-TRI procedure, the corresponding goal is to image the subsurface model anomalies that generated the scattered surface-wave observations. This method makes use of the well-known time-reversal property of the hyperbolic elastic wave equation, which allows wavefield solutions to be (approximately) calculated forward or backward in time using the observed data as boundary condition for reconstructing elastic wavefields throughout the model domain.

Algorithm 1 presents a pseudocode of the E-TRI framework used in this study. Starting at the maximum record time ($t = N\Delta t$), we iterate on the following three-step process at each time step: (1) inject the transmitted and backscattered data estimates into their respective wavefields; (2) backpropagate each wavefield by a single step ($-\Delta t$) in reverse time; and (3) apply an imaging condition using the two wavefields to image the scattering potential at each point in the model domain. This process is then repeated for all shot records in the data set (i.e., all events $e \in \mathbf{s}$).

The third pseudo-code step involves applying an elastic imaging condition that extracts transmission and scattered wavefield information to generate an image of the data event. Herein, we adopt the energy norm imaging condition

Algorithm 1 E-TRI pseudo-code (after Shragge et al., 2024)

P1. Initialize image $I_E(\mathbf{x}) = 0$
for $e = 1, E$ **do** ▷ Source loop
  P2. Initialize $\widetilde{u_i}(\mathbf{x}, N\Delta t) = \delta u_i(\mathbf{x}, N\Delta t) = 0$
  for $j = N, 1$ **do** ▷ Time loop
    1. Inject $\widetilde{d_i}(\mathbf{x}, j\Delta t, e)$ in $\widetilde{u_i}(\mathbf{x}, j\Delta t, e)$ at $z = 0$ m
    2. Inject $\delta d_i(x_i, j\Delta t, e)$ in $\delta u_i(\mathbf{x}, j\Delta t, e)$ at at $z = 0$ m
    3. Time step $\widetilde{u_i}(\mathbf{x}, j\Delta t, e)$ to $\widetilde{u_i}(\mathbf{x}, (j-1)\Delta t, e)$
    4. Time step $\delta u_i(\mathbf{x}, j\Delta t, e)$ to $\delta u_i(\mathbf{x}, (j-1)\Delta t, e)$
    5. Evaluate imaging condition to generate $I_E(\mathbf{x})$
  end for
end for

(ENIC) of Rocha et al. (2016) as presented by Shragge et al. (2024):

$$I_E(\mathbf{x}) = \sum_{\mathbf{s},t} \left\{ \rho(\mathbf{x})\, \tilde{u_i}(\mathbf{s}, \mathbf{x}, t)\, \delta u_i(\mathbf{s}, \mathbf{x}, t) - c_{ijkl}(\mathbf{x})\ (\partial_i \tilde{u_j}(\mathbf{s}, \mathbf{x}, t))\ (\partial_k \delta u_l(\mathbf{s}, \mathbf{x}, t)) \right\}, \tag{4}$$

where repeated indices indicate summation. Evaluation of this imaging condition generates a scalar image $I_E(\mathbf{x})$ from the vector wavefield inputs $\tilde{u_i}$ and δu_i. The first and second terms respectively represent cross-wavefield estimates of the kinetic and potential energy contributions and explicitly take into account medium properties ρ and c_{ijkl}. Finally, we make two additional observations: (1) an imaging condition other than the ENIC could be introduced in place of equation 4; and (2) the E-TRI approach is related to conventional reverse time migration (RTM); however, no forward simulation of a source wavefield is required before starting time-reversed propagation (Shragge et al., 2024).

4 E-TRI Synthetic Tests

We now test the E-TRI framework for small-scale void detection using a synthetic 1-D layered elastic Earth model (see Figure 2) adapted from Smith et al. (2019) with a small 2.0×2.0 m^2 void centered at $(x, z) = (0, 10)$ m as depicted in the V_S model shown in Figure 3. The model is sampled in both directions at uniform 0.1 m discretization intervals with lateral and depth dimensions of 320×192 m^2, which we then highly pad to minimize boundary related artifacts. We also use the smoothed 1-D reference elastic model without the void (i.e., the V_S model shown in Figure 2 sprayed laterally) for time-reverse wavefield backpropagation. Appendix A presents two additional examples of applying 2-D E-TRI to model scenarios involving a homogeneous background and uniform velocity gradients with depth.

We used the elastic model illustrated in Figure 3 to generate 2-D synthetic seismic data using a GPU-based elastic wave-equation solver in the Madagascar framework (Weiss and Shragge, 2013). Absorbing boundary conditions were applied at the side and bottom model edges, while the free-surface boundary condition was enforced at the top boundary. To model the air-filled void anomaly, we set the associated model parameters to $V_P = 330$ m/s, $V_S = 0$ m/s and $\rho = 0.1$ g/cc and did not explicitly enforce the internal free-surface boundary during simulation. Thus, while the forward-modeled data are not fully accurate in terms of representing the void anomaly, we found that the resulting synthetic data were sufficiently representative of field-data observations for E-TRI testing purposes.

We used an idealized dense receiver array of 144 receivers evenly spaced at 0.5 m intervals covering an aperture of 72.0 m centered over the modeled void anomaly with a maximum ± 36.0 m offset from the void. This array aperture allows for sufficient temporal separation of the outward-propagating transmission and inward-propagating scattered wavefield components. We simulated 36 shots at 2.0 m spacing along the receiver line using an impulsive vertically oriented force source; 18 shot points were used on each side of the anomaly between 36.0-72.0 m absolute source offsets from the void. We used an Ormsby wavelet as the source-time function and applied Kolmogoff spectral factorization (Claerbout, 2014) to generate a minimum-phase wavelet that better represented a weight drop or hammer seismic source. Simulations were done with 10-50 Hz and 5-35 Hz wavelet flat spectrum frequency bands (with appropriate frequency roll-off) to facilitate comparison of the efficiency of surface-wave backscattering from the 2.0 m-scale void heterogeneity at dominant seismic wavelengths ranging from $0.10\lambda_P$ for 35 Hz P-waves to $0.26\lambda_R$ for 50 Hz Rayleigh waves. (Table 1 analyzes the different mode wavelengths for the two different scenarios.) The upper and lower left panels of Figure 4 show representative synthetic shot gathers using the 10-50 Hz and 5-35 Hz Ormsby wavelets. Each shot gather exhibits surface-wave energy backscattered off the void anomaly, with fewer but stronger reflections and scattered energy in the lower-frequency shot gathers. (Figure 4).

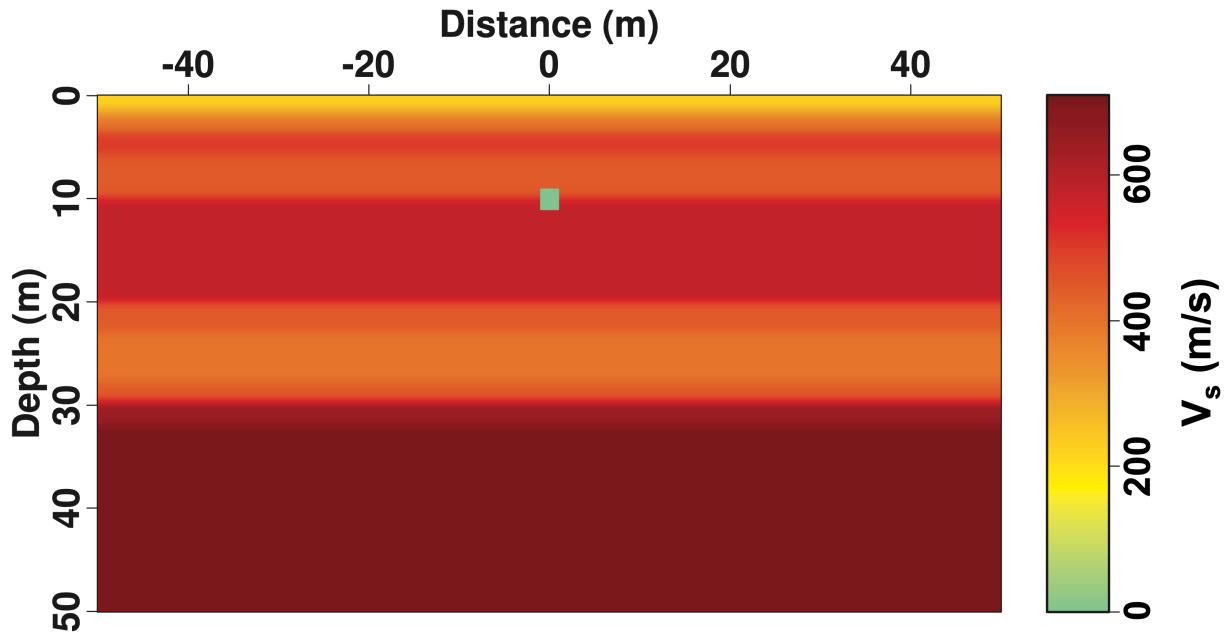

Figure 3: 2-D synthetic YPG model adapted from Smith et al. (2019) using V_S velocities from Figure 2 with a 2.0 m $\times$ 2.0 m square void (green) located at coordinates $(x, z) = (0, 10)$ m.

Parameter	Average Velocity in top 10 m (m/s)	Wavelength (λ_i) at 35 Hz (m) [Void size fraction]	Wavelength (λ_i) at 50 Hz (m) [Void size fraction]
V_P	715	20.4 $[0.10\,\lambda_P]$	14.3 $[0.14\,\lambda_P]$
V_S	420	12.0 $[0.17\,\lambda_S]$	8.4 $[0.24\,\lambda_S]$
V_R	380	10.8 $[0.19\,\lambda_R]$	7.6 $[0.26\,\lambda_R]$

Table 1: Average model velocities in the top 10 m along with the corresponding wavelengths λ_i of wave modes $i = P, S, R$ at 35 Hz and 50 Hz maximum dominant frequencies. The Rayleigh-wave velocity is estimated assuming $V_R = 0.91V_S$. The values in the square brackets show the ratio of the 2.0 m void size to the different mode wavelengths λ_i.

4.1 Transmitted-Scattered Wavefield Separation

The transmitted-scattered wavefield separation approach followed by Shragge et al. (2024) recovered estimates of $\tilde{d}_1$ and δd_1 by applying a surgical inner mute filter in the $t - x$ domain. While this filtering approach worked well for scenarios where backscattered surface-wave and transmitted arrivals do not overlap, more advanced methods are required when the scattered and transmitted wave arrivals overlap - though with opposing dip structure. Due to the layered stratigraphy in this YPG elastic test model, the backscattered energy observed in the left panels of Figure 4 clearly arrives at similar times as body-wave reflections from deeper layers. Previous wavefield separation methods used on the 2-D and 3-D datasets acquired at the YPG void site included applying an $f - k$ filter in the dual frequency-wavenumber domain (Schwenk et al., 2016; Peterie et al., 2020). The benefit of applying the $f - k$ filtering technique is that it can represent a directional mute to effectively separate the inward-propagating backscattered wavefield from the dominant outward-propagating transmitted wavefield.

Figure 5 presents an example of the applying $f - k$ filtering to a single receiver line extracted from a representative field data shot gather is shown in Figure 5a. Figure 5b presents the $f - k$ magnitude spectrum of the full shot gather after applying a 2-D Fourier transform. The negative and positive wavenumber spectrum components represent the stronger outward transmitted and weaker inward backscattered wavefield dip contributions, respectively. Figure 5c

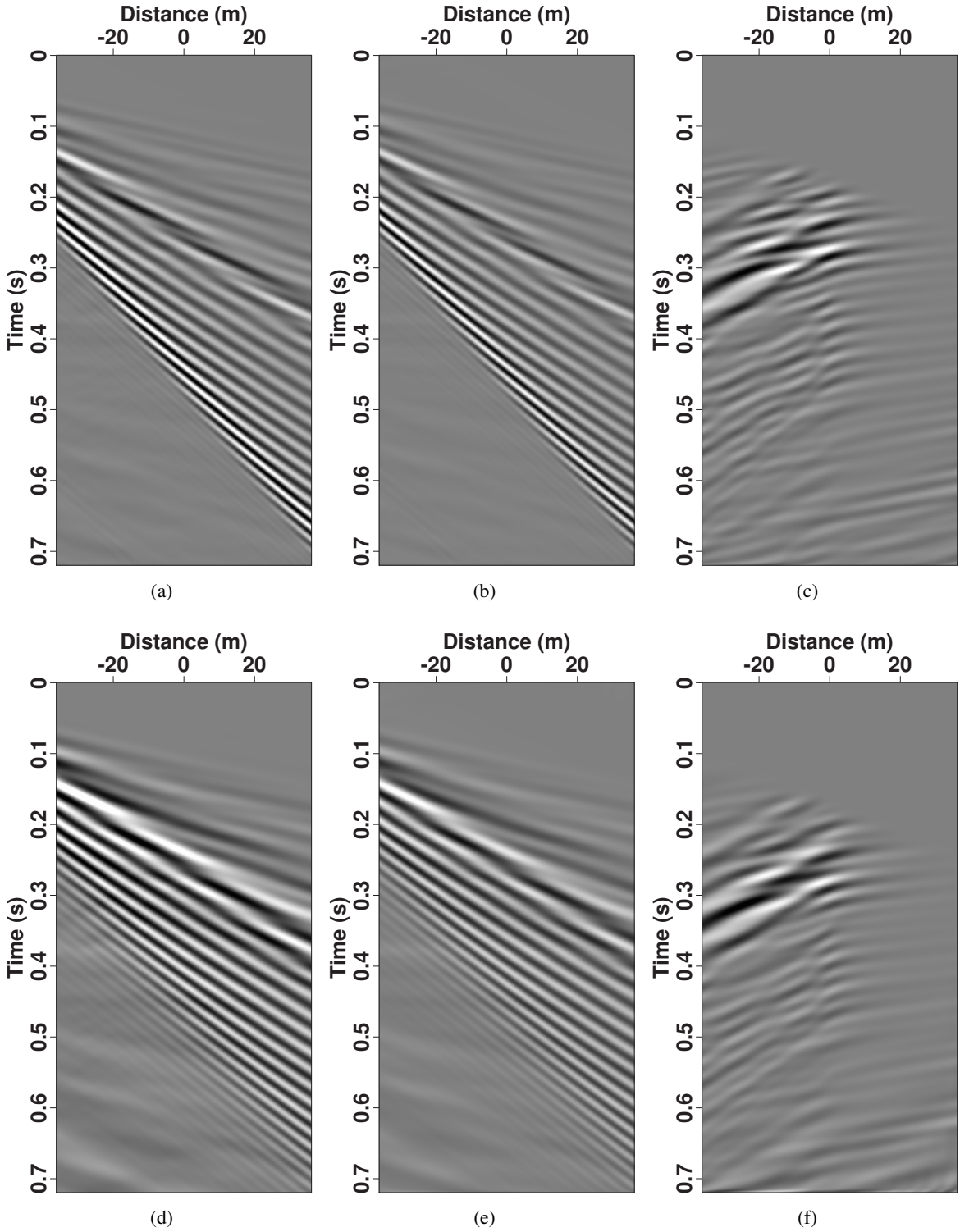

Figure 4: Synthetic shot gathers for a source point located 30 m offset from the void placed at 10 m depth. The rows respectively show (a-c) 10-50 Hz and (d-f) 5-35 Hz Ormsby wavelet source modeling results. The shot gathers d_1 (left) are separated into transmission $\tilde{d}_1$ (middle) and backscattered δd_1 (right) data estimates. Backscattered surface-wave energy is clearly visible post-separation.

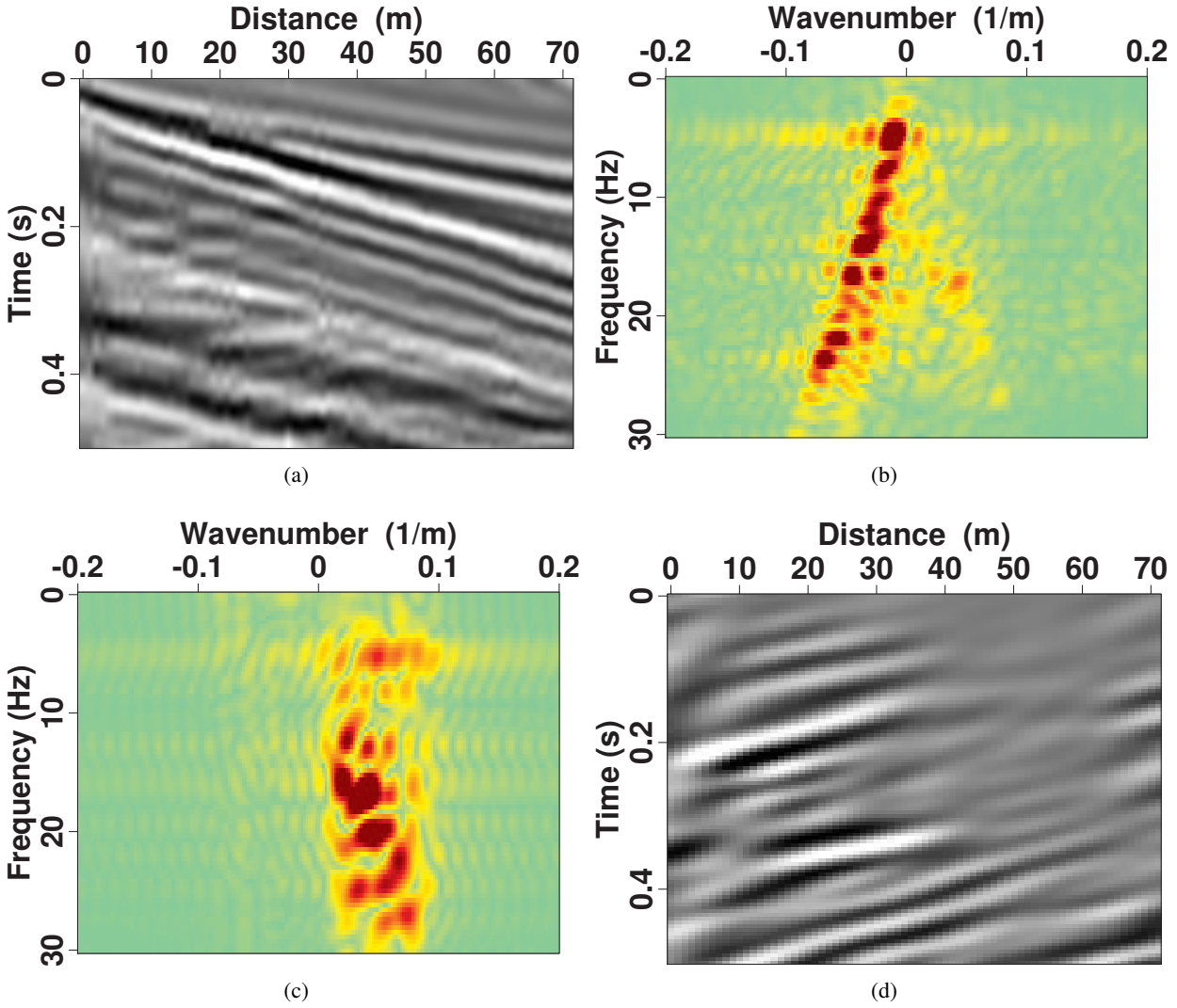

Figure 5: Wavefield separation example of applying a directional mute in the $f-k$ domain to representative shot gather data. Steps of separation are (a) 2-D Fourier transforming the full $t-x$ shot gather into (b) the $f-k$ domain, (c) applying the directional mute to the negative wavenumbers, and then (d) computing the 2-D inverse Fourier transform to recover the backscattered wavefield energy estimate in the $t-x$ domain.

presents the filtered $f-k$ spectrum after muting out the right-dipping events, while Figure 5d shows the corresponding $t-x$ data panel after applying an inverse 2-D Fourier transform to the filtered data. We note that this panel has only left-dipping backscattered wavefield events after applying the $f-k$ dip-filtering sequence. Finally, the complement to the mask applied in Figure 5c would isolate the right-dipping transmitted wavefield contributions to leave only the backscattered wavefield data shown in Figure 5d.

The center and right column panels of Figure 4 respectively show examples of the transmitted $\tilde{d}_1$ and scattered δd_1 data estimates from the synthetic shot gathers separated through $f-k$ dip filtering. (The subscript $i=1$ here indicates that vertical-component data are being processed.) Note that these panels do not contain purely surface-waves modes; rather, they are a combination of different elastic wave modes, all of which potentially can be used to reconstruct the transmitted and backscattered wavefields. We applied the same directional $f-k$ filter to all synthetic shot gathers to generate the transmission and backscattered data sets required to generate the wavefields used in the E-TRI imaging process outlined in Algorithm 1.

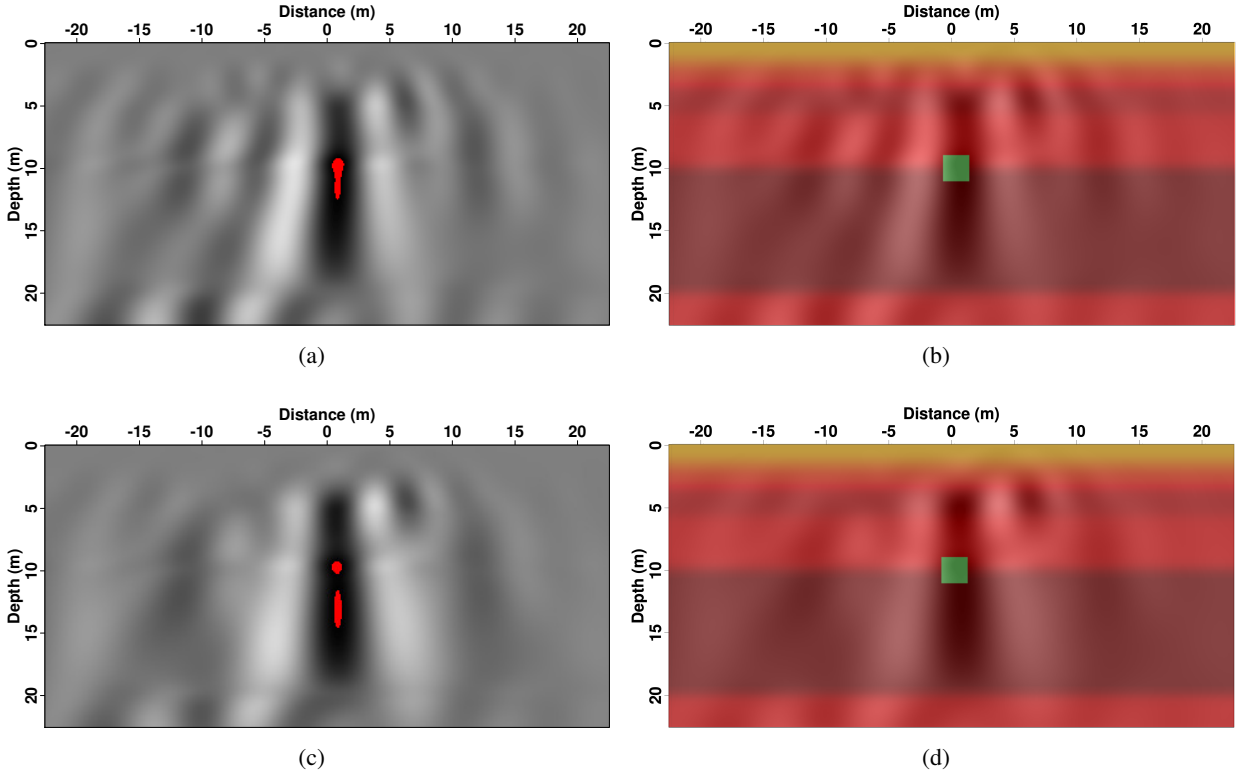

Figure 6: Synthetic E-TRI test results for the (top) 10-50 Hz and (bottom) 5-35 Hz wavelet tests. Left column: Image I_E formed by applying the E-TRI framework for all 36 shots. The red-shaded regions in left column correspond to image amplitudes higher than the applied 99.85% percentile clip. Right column: Image-Earth model overlay highlighting lateral locational accuracy of the imaged void anomaly.

4.2 2-D Frequency Tests

To examine the similarities and differences associated with E-TRI with different frequency bands, we conducted tests on the YPG model (Figure 3), with the void placed at a depth of 10 m in both tests, using the two 10-50 Hz and 5-35 Hz Ormsby wavelets. The upper and lower panels of Figure 6 respectively display the stacked E-TRI results I_E for the 10-50 Hz and 5-35 Hz frequency tests. The time-reverse wavefield propagation and energy-norm imaging condition computed via equation 4 used a smoothed 1-D Earth model with the void anomaly removed (see V_s model in Figure 3b). Both images clearly detect and accurately laterally position the void anomaly located at $x = 0$ m, as indicated by the red clipped regions roughly centered at 10 m depth in Figures 6a and 6c. However, the E-TRI framework recovers a stretched anomaly in depth, indicating a more limited vertical resolution capability and suggesting the need for further depth sensitivity testing.

Although both the higher- and lower-frequency data images exhibit a high-amplitude event directly over the void location but smeared in depth, the imaged anomaly is laterally narrower due to the higher-frequency content. Minor artifacts appear in both images, though to a lesser degree in the lower-frequency image. Despite more artifacts, the higher-frequency image arguably provides better depth constraints for the void anomaly. We note that the central frequency range of many near-surface seismic data sets falls within 25-40 Hz (Peterie et al., 2020; Smith et al., 2019), including the datasets collected at the YPG test site. Thus, we expect that the lower-frequency test scenario will be more representative of field data scenarios, and that any observed backscattered contributions in this frequency band likely will be dominated by surface-wave rather than body-wave energy.

4.3 2-D Depth Tests

Depth tests were also performed on the YPG model (Figure 3) with the void placed at a range of depths. The rows of Figure 7 display the stacked E-TRI results I_E for five detection test scenarios for a target situated at depths of

$z = 5.0, 7.5, 10.0, 12.5$ and 15.0 m. All E-TRI tests were conducted using the 10-50 Hz Ormsby wavelet, time-reverse wave propagation through a smoothed 1-D Earth model (i.e., with no anomaly present), and the ENIC of equation 4. All images clearly detect and accurately laterally image the void anomaly at $x = 0$ m. The highest image amplitudes (again highlighted as red-clipped regions) are focused at roughly the correct depth in all images; however, the lateral smearing and number of artifacts generally increase with target depth. Some artifacts may be attributed to the complexity of the background 1-D elastic model, as targets introduced in a slow velocity layer between faster strata generate different artifacts compared to void anomalies placed in thicker and faster layers. The imaged target zone also tends to broaden with depth, an observation that is consistent with the results of E-TRI testing in the homogeneous and uniform velocity gradient Earth models presented in Appendix A.

5 Yuma Proving Ground Case Study

We next test the 3-D E-TRI framework in a field data study using the vertical-component geophone data acquired at the YPG test site. Figure 8 shows four representative shot gathers from different locations that exhibit visible surface-wave backscattering (indicated by the red ovals) within the selected 0.8 s window. Surface waves are considered to be the strongest contribution to vertical-component YPG seismic data in the sub-20 Hz range (Smith et al., 2019)m with body waves increasingly present above 40 Hz (Morton et al., 2016). Accordingly, we applied a 5-40 Hz band-pass filter during preprocessing to isolate and improve the S/N of surface-wave energy. Tests with more broadband frequency content above 40 Hz were found to generate too much ringing in the resulting E-TRI images within this specific dataset. After initial band-pass filtering, the acquired 3-D shot gathers were preprocessed similar to the $f - k$ dip-filtering-based separation workflow used in the synthetic 2-D data example. We found that applying the 2-D $f - k$ dip filtering sequentially to each 72-geophone receiver inline in a 3-D shot gather was sufficient for generating accurate backscattered surface-wave volume estimates. This sequential processing workflow was repeated for all 654 3-D shot gathers to generate the transmission and backscattered data volumes required for the E-TRI analysis.

Figure 9 shows two receiver lines extracted from representative 3-D shot gathers. These examples are inline and oblique to the displayed receiver lines, with shot points located on either side of the void anomaly. The left panels of Figure 9 show shot gathers after applying a 5-40 Hz band-pass filter and windowed to the positive or negative side of the inline shot location. The center panels show the estimated transmission data $\tilde{d}_1$ after using $f - k$ dip filtering to separate the outward- and inward-propagating wavefield arrivals. Similarly, the right panels present the backscattered data estimates δd_1 that now more clearly show the inward-dipping scattered wavefield events.

We applied the E-TRI procedure to all 654 3-D shot gathers over the full recording array. A 1-D model estimate was used for synthetic tests (see, e.g., the V_s model in Figure 1b) and sprayed outward in both lateral directions to create the 3-D Earth model for time-reverse wavefield propagation. Figure 10a shows the E-TRI results while Figure 11 shows a map view of the final image (extracted at 6.5 m depth) superposed over the geophone array and the shown orientation of the long linear void. Although several weaker artifacts are present, the imaged energy clearly detects and spatially accurately locates the void anomaly to within ± 1.0 m of the known location.

We repeated the E-TRI analysis, but this time retaining only 10% of the shot gathers by using sources spaced every 10 m in the inline and 8 m in the crossline directions. Figure 10b presents the resulting 3-D image that again clearly shows the lateral location of the void space with only moderately higher-amplitude background artifacts present. This suggests that an E-TRI analysis on a YPG data set acquired at an even coarser source and receiver spacing could have yielded interpretable results, which may have important implications for the efficiency and/or field acquisition design of future 3-D near-surface seismic surveys.

6 Discussion

The 2-D synthetic and 3-D field data tests demonstrate that the E-TRI framework can successfully detect near-surface heterogeneities smaller than the given wavelength (Table 1). In this section, we discuss issues related to computational run-time considerations, depth sensitivity, and the general extensibility of the E-TRI method.

6.1 Run-time Considerations

The computational tasks associated with the full 3-D field data test initially were completed in less than 4 hours on a single NVidia V100 GPU card. The run time was then reduced to about 60 minutes when applying parallelization across the source crosslines axis to spread computations across the four NVidia V100 GPUs housed within a single compute node. Furthermore, computational run times to approximately 12 minutes in the data parallelized scenarios

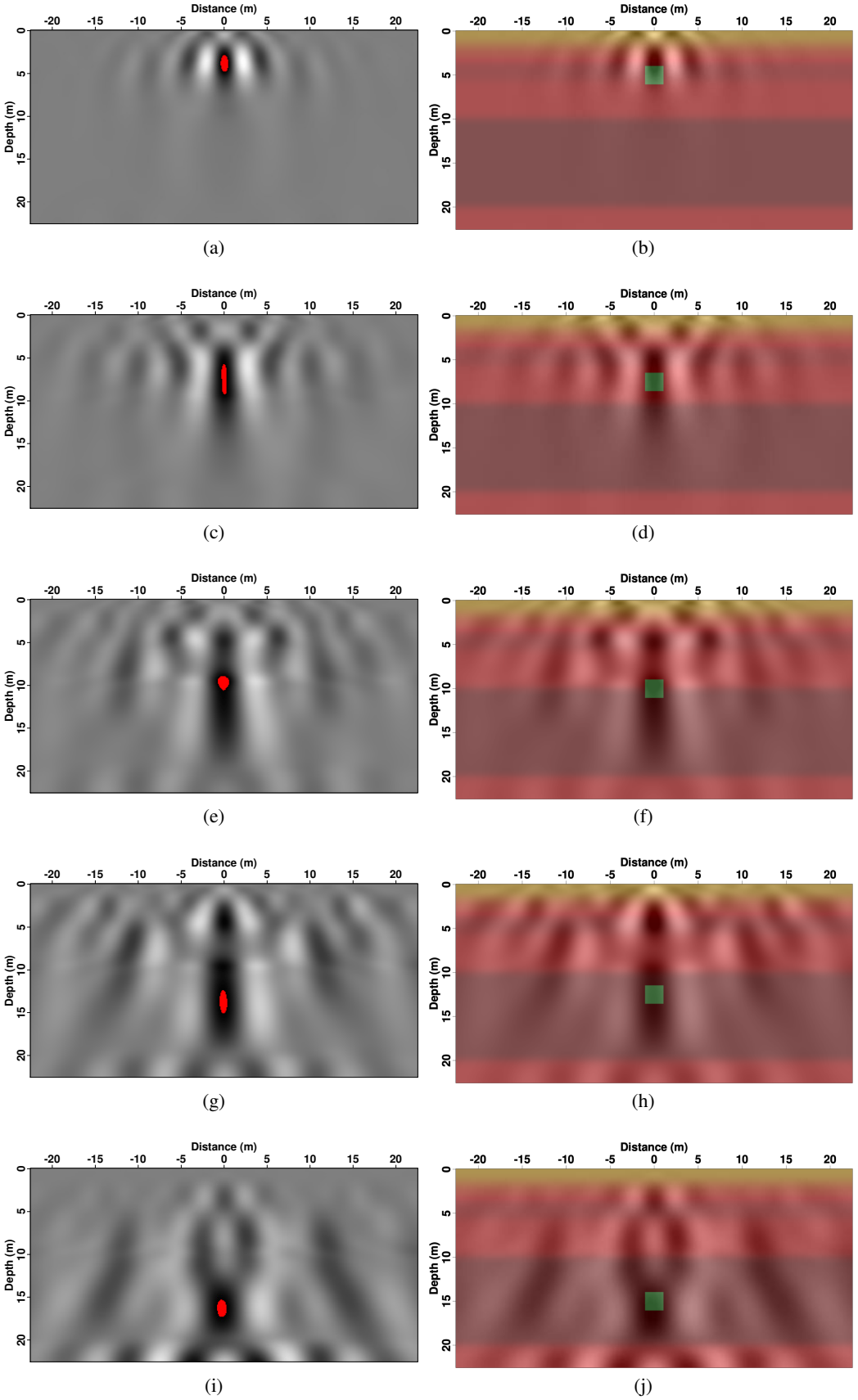

Figure 7: 2-D depth test images (left column) for 2.0 m×2.0 m void placed at different depths along with (right column) an overlay of the associated model: (a-b) 5.0 m; (c-d) 7.5 m; (e-f) 10.0 m; (g-h) 12.5 m; and (i-j) 15.0 m. The red-shaded regions in the left column images correspond to amplitudes higher than the applied 99.85% percentile clip.

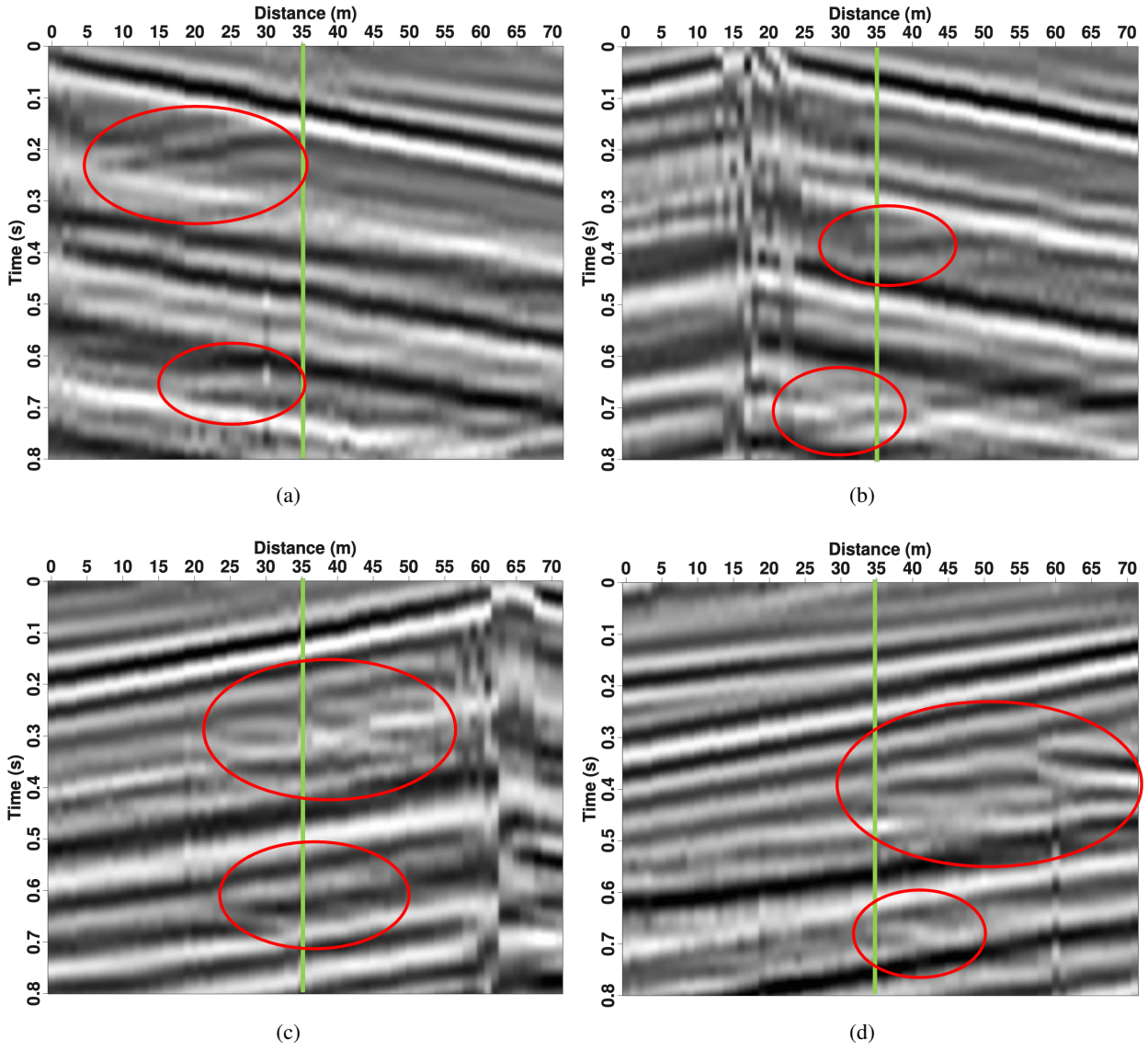

Figure 8: Shot gathers illustrating the backscattered surface-wave energy present in the dataset. Gathers were acquired at the following distances with respect to the anomaly: (a) 35 m left, (b) 20 m left, (c) 30 m right, and (d) 60 m right. The red circles indicate the most prominent backscattered events, while the green line shows the lateral coordinate of the void anomaly.

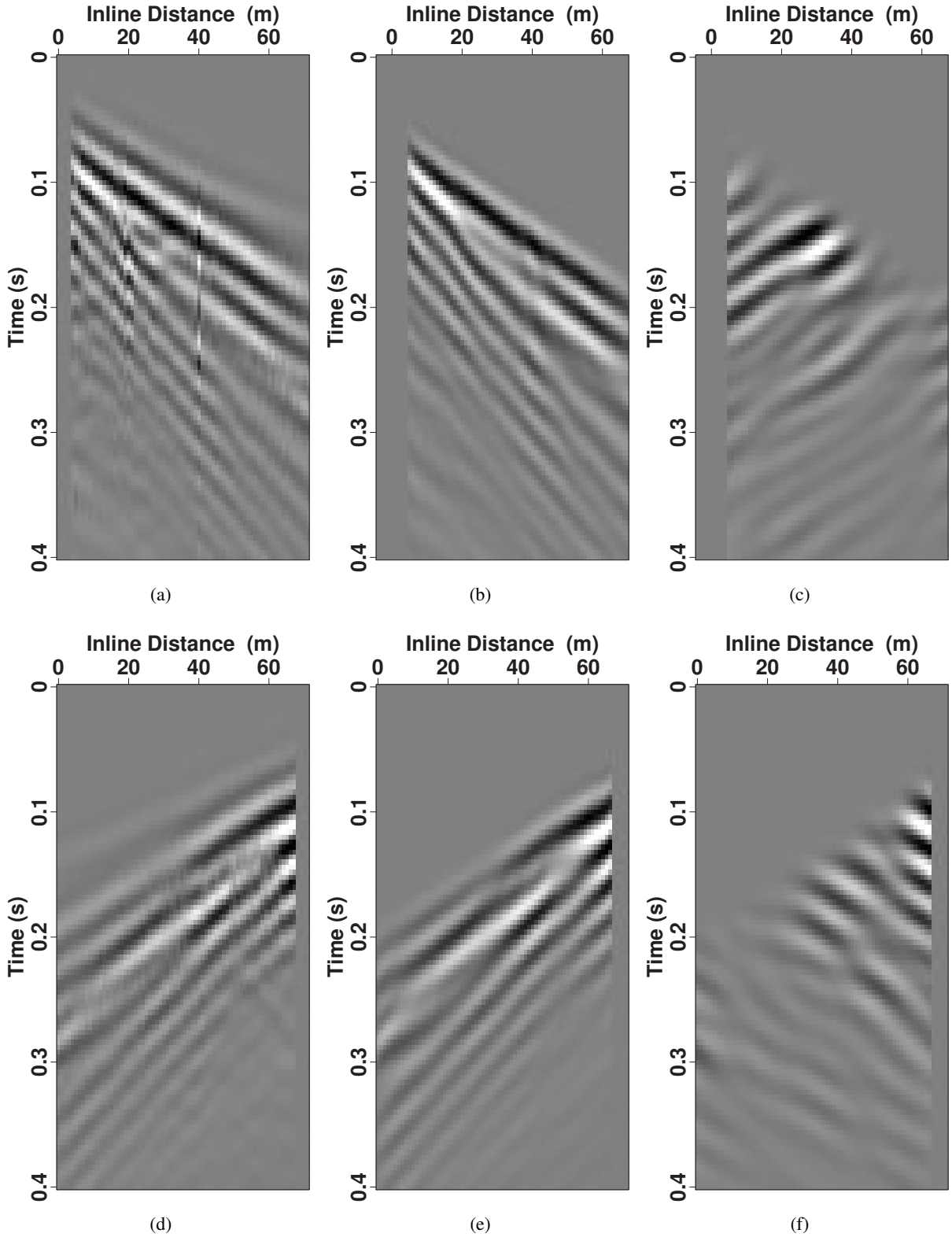

Figure 9: Two representative shot gathers acquired on (a-c) inline and (d-f) oblique receiver lines. (Left) Full shot gathers after applying 5-40 Hz band-pass filtering. Processed transmission d_1 (center) and scattered δd_1 (right) data estimates.

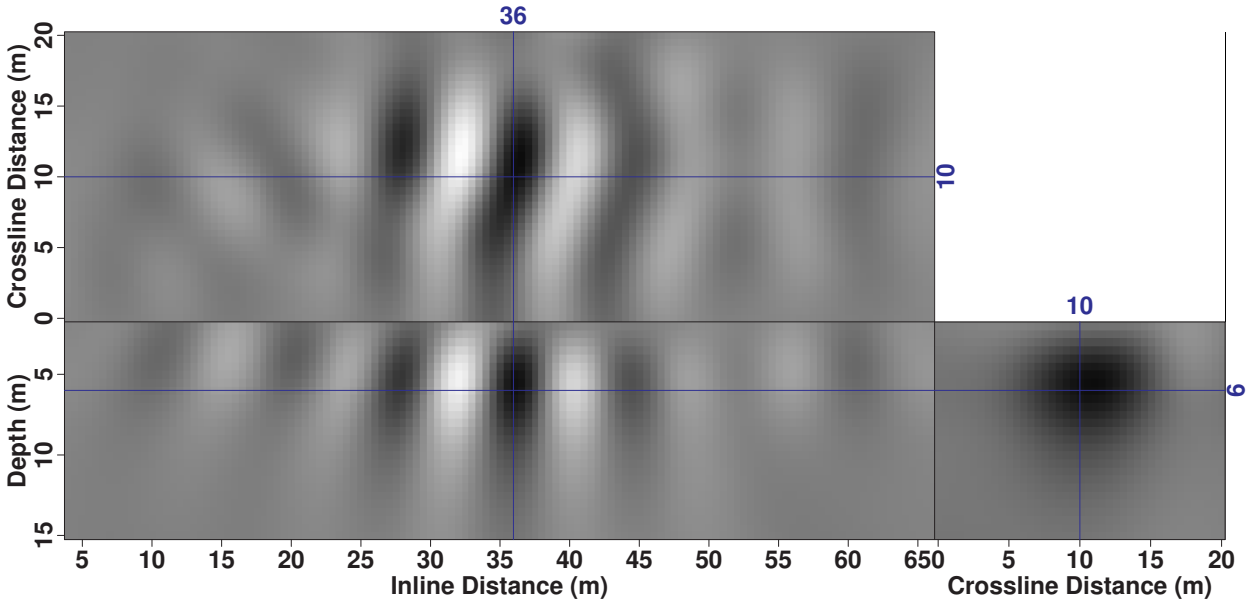

(a)

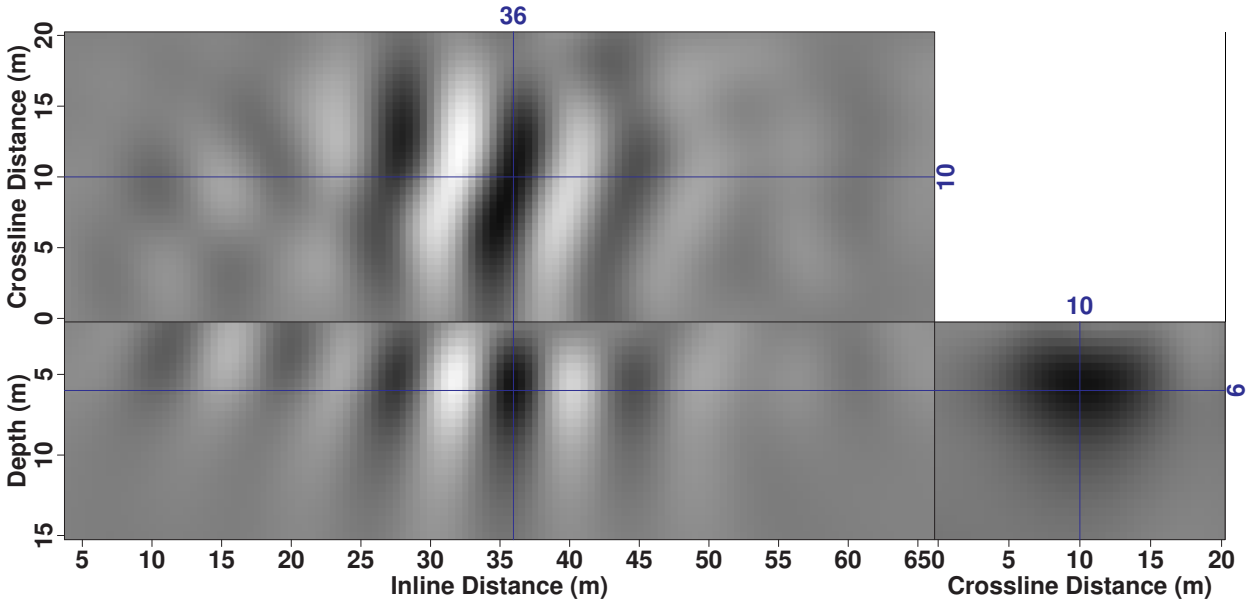

(b)

Figure 10: Stacked 3-D E-TRI image using (a) 654 and (b) 130 source points. The latter represents 20% of all 3-D shot gathers with sources spaced every 10.0 m in the inline and 8.0 m in the crossline dimensions.

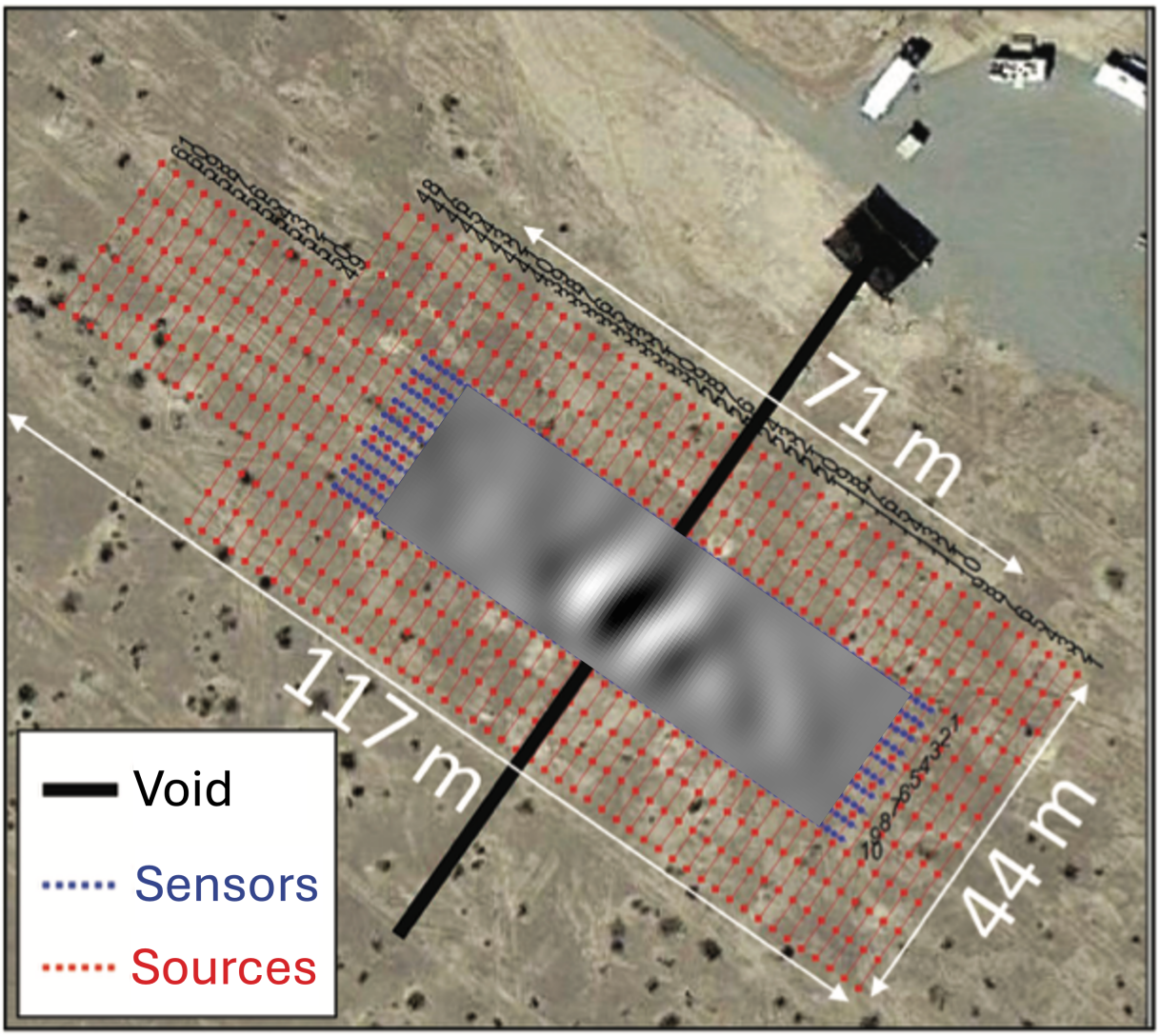

Figure 11: Overlay of horizontal section of 3-D E-TRI result on source-receiver array from Figure 1.

when using only 10% of the sources (Figure 10b). These compute times are significantly lower than other reported full-wavefield elastic seismic void detection methods (see, e.g., Smith et al., 2019).

Compared to elastic RTM or E-FWI approaches, the E-TRI framework does not require forward modeling, memory storage, or the reconstruction of source wavefields. This benefit decreases the required computation and memory complexity, making E-TRI a computationally cost-effective void detection approach in terms of runtime and memory storage capacity. We note that the reported run times likely would be significantly longer on CPU hardware or when using smaller laptops during field-based operations or other instances where GPUs are not available.

6.2 Depth sensitivity considerations

Although all tests showed the potential for constraining the lateral location of the void anomaly, there is still uncertainty in the depth constraints realizable by the E-TRI method. This is similar to the results of Shragge et al. (2024) where the lateral positions of anomalies were consistent with observed surface-wave scattering, but the depth expression of the imaged anomalies was uncertain. Similarly, the layer-media models presented herein offered improved depth constraints (Figure 7) compared to the homogeneous and vertical gradient models presented in Appendix A, with the

majority of energy focused at or near the true anomaly depth. Scenarios where the anomaly was placed at greater depth exhibited additional and stronger artifacts along with increased vertical smearing of the imaged target zone. In contrast, the homogeneous or gradient model test results presented in Appendix A suggest that E-TRI offers only weak depth constraints for scenarios where surface waves exhibit weak-to-no dispersion. This connection between surface-wave dispersion and depth sensitivity, though, is fully consistent with standard surface-wave theory (Aki and Richards, 2002).

In addition, imaged artifacts may be the result of cross-mode correlations between surface-wave energy and body waves reflected within the surrounding layered media. This supposition is consistent with the observed reduction in the number and intensity of artifacts in the lower-frequency images where the longer body-wave wavelengths are less likely to generate scattering associated with the void (see Table 1).

Finally, we note that the accuracy in the synthetic test depth constraints was not fully realized in the 3-D YGP field data test. Although our analysis detected the lateral location of the void anomaly within ± 1 m of the true location, the predicted 6.5 m depth was much closer to the surface than the known void depth. Similarly, the void anomaly was stretched vertically and thus exaggerated the associated depth expression of the void. Future work will aim to develop novel imaging conditions capable of generating more robust E-TRI depth constraints.

6.3 Extensibility of the Method

Overall, the E-TRI framework proved useful for void detection purposes in synthetic experiments and at the YPG field site. Thus, this method is likely applicable in other small-scale lateral heterogeneity detection scenarios. Other potential applications include detecting abandoned infrastructure (e.g., pipelines and storage tanks), along with potentially harder-to-detect heterogeneities such as in zones of high landslide risk or seepage problems. There is also a potential for applying E-TRI to distributed acoustic sensing (DAS) infrastructure analyses, using either targeted or so-called dark fiber deployments. However, there may be challenges associated with significantly weaker backscattered surface-wave energy in any of those scenarios, and would require further testing.

7 Conclusions

This paper presents a case history of using elastic time reverse imaging (E-TRI) as an alternative to previously proposed methods for detecting near-surface void spaces. A key step is the separation of the outward-propagating transmission and backpropagating backscattered data components and then using them in the E-TRI framework to image the locations of subsurface heterogeneity causing the observed surface-wave scattering. The 2-D synthetic data example demonstrates the ability of the E-TRI framework to detect lateral heterogeneities smaller than the given wavelength using a reasonably smoothed background model derived from previous seismic analyses at the Yuma Proving Ground (YPG) field site. The 2-D synthetic frequency tests show that the void is detectable with both higher- and lower-frequency ranges commonly found in near-surface seismic surveying. Increased vertical smearing but a reduced number and intensity of artifacts were noted in the lower-frequency imaging test compared to the higher-frequency examples. The synthetic depth tests demonstrated that, despite additional smearing with increasing embedding depth, lateral constraints remained consistently accurate. The YPG 3-D field data example demonstrated a strong correlation in the lateral location of the long linear void anomaly. The 3-D E-TRI analysis detected the void within ± 1 m of the true lateral location; however, the method offers limited constraints on the void depth, suggesting that it was shallower than the true depth (6.5 m versus 10.0 m). We speculate that other imaging conditions could be developed to provide more robust depth constraints, particularly those making use of surface-wave dispersion properties expressed in depth-sensitivity kernels. Overall, these results suggest that an E-TRI framework - perhaps with an imaging condition capable of producing more robust vertical constraints - could become a viable near-surface detection method for voids and other shallow small-scale lateral heterogeneities along with other types of near-surface seismic investigations.

Additional 2-D E-TRI Examples

We conducted additional 2-D E-TRI depth tests using a homogeneous (Figures A-1 and A-2) and a vertical-gradient (Figure A-3) background model. These examples further illustrate the capability of E-TRI for more straightforward models that do not introduce the additional complexity of intra-layer reflectivity. We observe a simplified shot gather (Figure A-1a) with backscattered energy that is easily separable from the direct-wave arrivals through $f - k$ domain dip filtering.

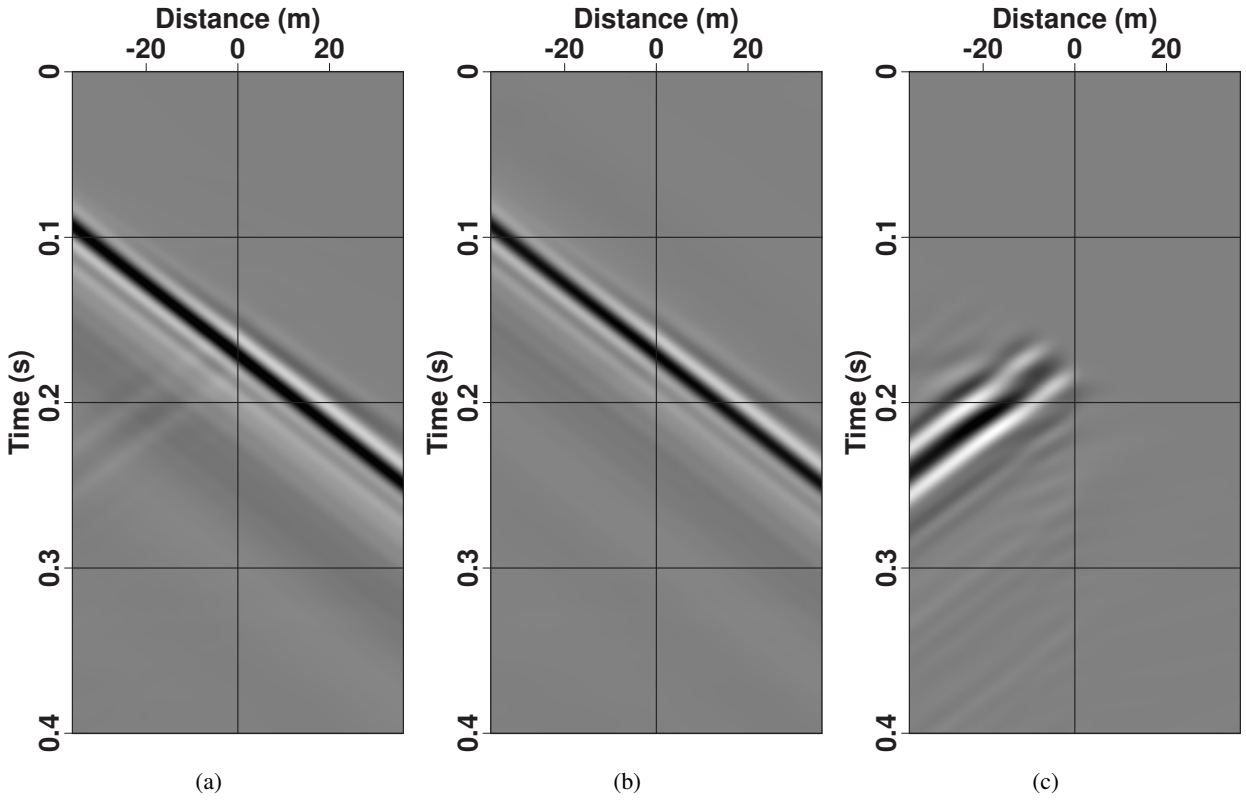

Figure A-1: Synthetic vertical-component shot gathers for a source point located 30 m offset from the void placed at 10 m depth in a homogeneous media. The (a) simulated shot gather d_1 is separated into (b) transmission $\tilde{d}_1$ and (c) backscattered δd_1 data estimates.

Similar to the previously discussed five depth tests, the void targets were again placed at depths of $5.0, 7.5, 10.0, 12.5$ and 15.0 m. All tests are carried out using the same procedure as used to generate the results shown in Figure 7. Figures A-2 and A-3 show the 2-D E-TRI with the same layout as used in Figure 7. All images clearly detect and accurately laterally image the void with the highest energy percentile (red clipped region) in both depth tests at $x = 0$ m. Despite the variable experimental void depths, the highest percentile energy remains confined to about 6.5 ± 1.0 m depth. As the void depth increases, we observe a broadening of the imaged anomaly along with smearing vertically in both scenarios. Unlike the layered background models in Figure 7, the E-TRI framework provides only limited depth constraints. In fact, the images display similar results at most tested depths. These results suggest that increased surface-wave dispersion may lead to more accurate depth estimates.

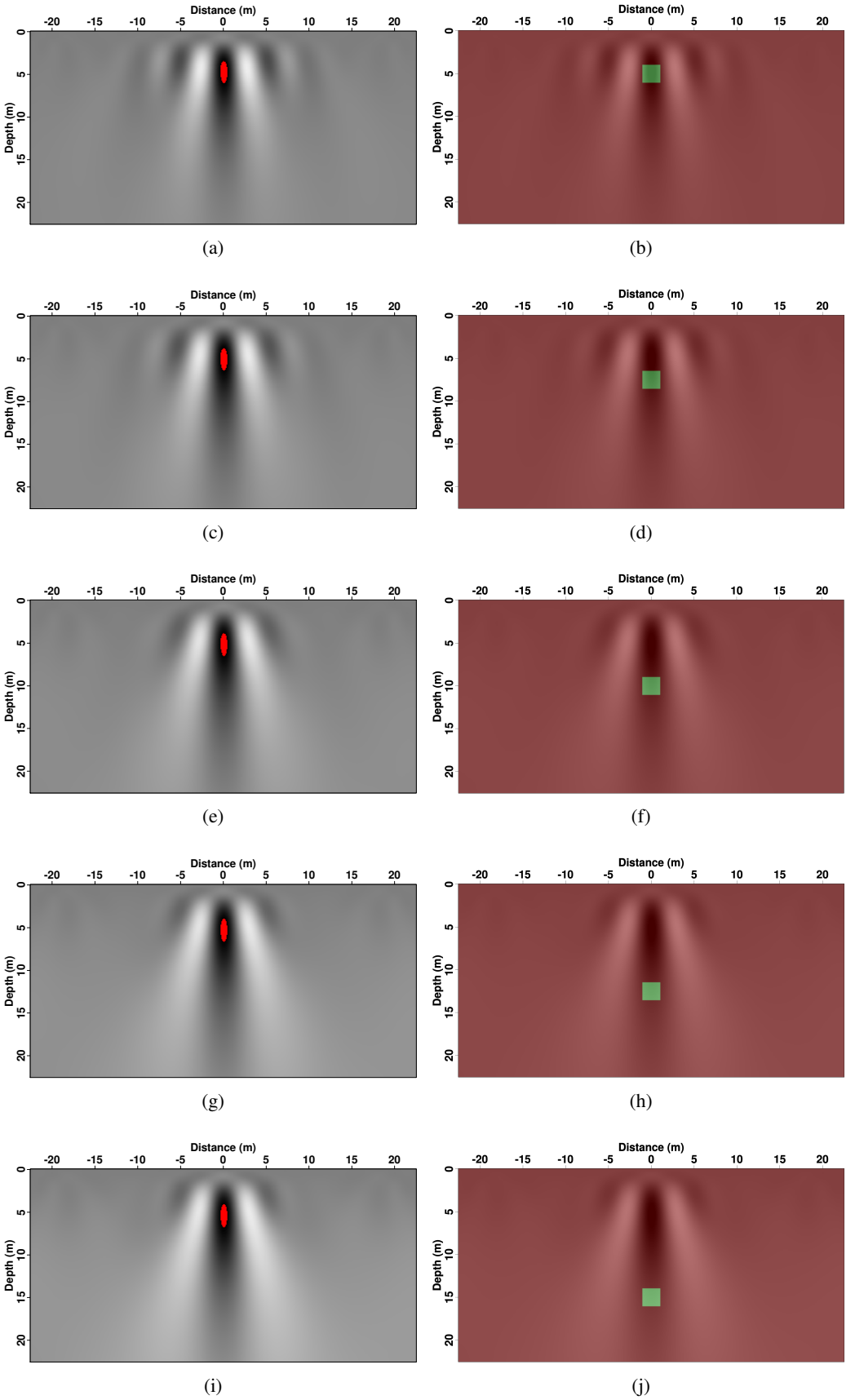

Figure A-2: 2-D images for (left) a void placed in a homogeneous media at different depths with (right) an overlay of the associated model: (a-b) 5.0 m; (c-d) 7.5 m; (e-f) 10.0 m; (g-h) 12.5 m; and (i-j) 15.0 m. The red-shaded regions correspond to image amplitudes higher than the applied 99.85% percentile clip.

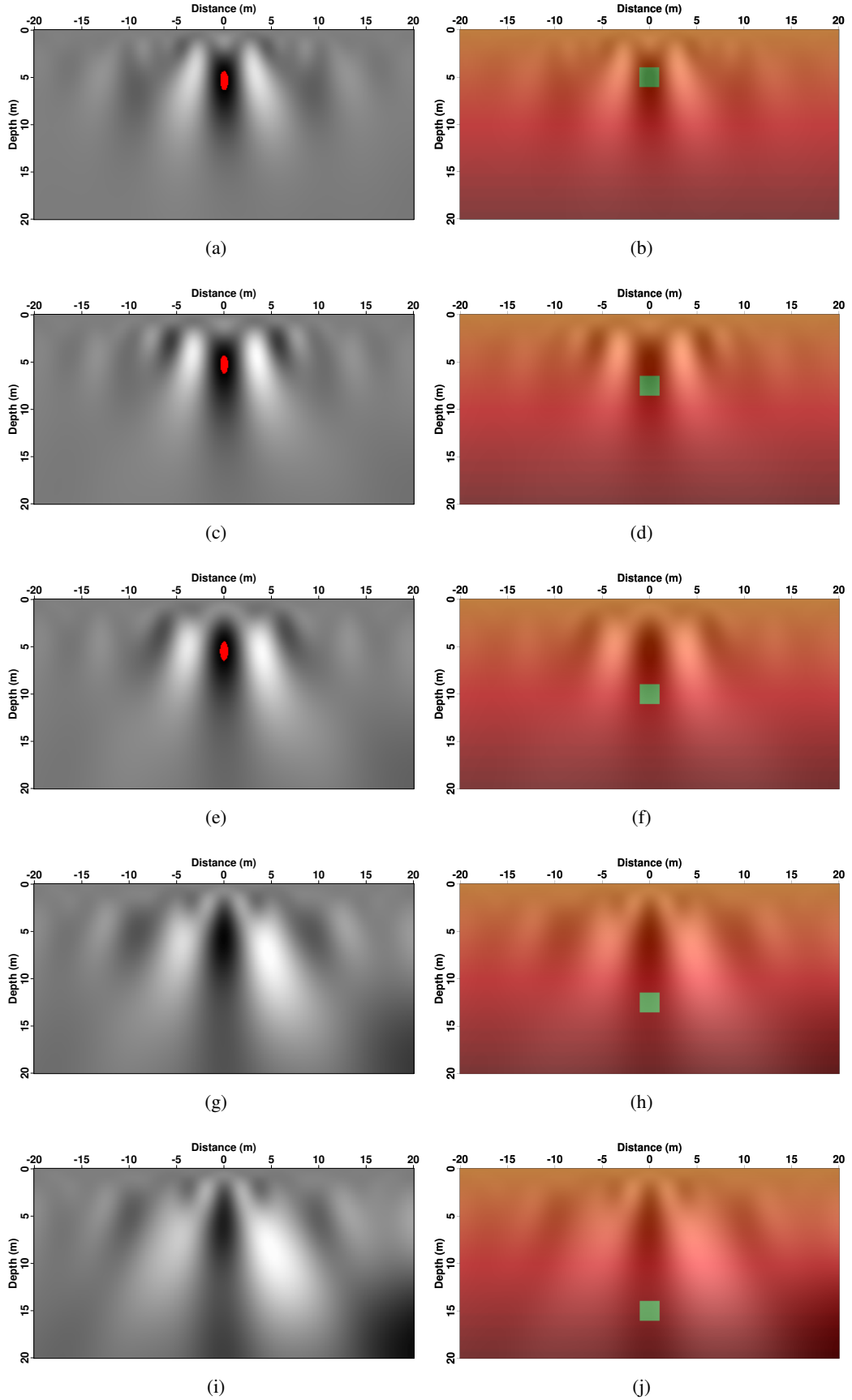

Figure A-3: 2-D images for (left) a void placed at different depths in a medium with smooth vertical velocity gradients ($V_P = 700 + 20z$ m/s and $V_S = 400 + 20z$ between 0-40 m depth) along with (right) an overlay of the associated model: (a-b) 5.0 m; (c-d) 7.5 m; (e-f) 10.0 m; (g-h) 12.5 m; and (i-j) 15.0 m. The red-shaded regions correspond to image amplitudes higher than the applied 99.85% percentile clip.

References

Aki, k., and P. G. Richards, 2002, Quantitative Seismology, 2nd ed.: University Science Books.

Artman, B., I. Podladtchikov, and B. Witten, 2010, Source location using time-reverse imaging: Geophysical Prospecting, **58**, 861–873.

Ballard, R. F., Y. Cuenod, and J. P. Jenni, 1982, Detection of karst cavities by geophysical methods: Bulletin of the International Association of Engineering Geology, **26-27**, 153–157.

Billington, E. D., R. J. Palm, and A. T. Grosser, 2006, MASW Imaging of an Abandoned Minnesota Mine: Symposium on the Application of Geophysics to Engineering and Environmental Problems 2006, Environment and Engineering Geophysical Society, 482–491.

Boiero, D., and L. V. Socco, 2011, The meaning of surface wave dispersion curves in weakly laterally varying structures: Near Surface Geophysics, **9**, 561–570.

Borisov, D., J. Smith, J. Tromp, R. Miller, S. Peterie, H. Cudney, S. Sloan, and M. Moran, 2017, Multi-component 3D Elastic Full Waveform Inversion Using Surface and Body Waves for Detecting Near Surface Anomalies: Presented at the SEG Technical Program Expanded Abstracts 2017.

Borisov, D., Y. Zhang, S. Abbasi, J. Ivanov, S. D. Sloan, and R. D. Miller, 2025, Using Deep Learning for Data-Driven Seismic Velocity and Source Wavelet Inversion: IEEE Geoscience and Remote Sensing Letters, **22**, 1–5.

Cardarelli, E., M. Cercato, A. Cerreto, and G. Di Filippo, 2010, Electrical resistivity and seismic refraction tomography to detect buried cavities: Geophysical Prospecting, **58**, 685–695.

Chambers, K., B. D. Dando, G. A. Jones, R. Velasco, and S. A. Wilson, 2014, Moment tensor migration imaging: Geophysical Prospecting, **62**, 879–896.

Claerbout, J., 2014, Geophysical image estimation by example: Stanford University.

Douma, J., and R. Snieder, 2014, Focusing of elastic waves for microseismic imaging: Geophysical Journal International, **200**, 390–401.

Gajewski, D., and E. Tessmer, 2005, Reverse modelling for seismic event characterization: Geophysical Journal International, **163**, 276–284.

Ivanov, J., B. Leitner, W. Shefchik, J. T. Shwenk, and S. L. Peterie, 2013, Evaluating hazards at salt cavern sites using multichannel analysis of surface waves: The Leading Edge, **32**, 298–305.

Ivanov, J., R. Miller, and S. Peterie, 2016, Detecting and delineating voids and mines using surface-wave methods in Galena, Kansas: SEG Technical Program Expanded Abstracts 2016, Society of Exploration Geophysicists, 2344–2350.

Ivanov, J., C. B. Park, R. D. Miller, and J. Xia, 2005, Analyzing and Filtering Surface-Wave Energy By Muting Shot Gathers: Journal of Environmental and Engineering Geophysics, **10**, 307–322.

Ivanov, J., S. Peterie, R. D. Miller, D. Borisov, and S. Sloan, 2024, Enhanced converted-surface-wave imaging (CSWI) method for the detection of an elongated empty space using challenging seismic data collected at a desert site: Seventh International Conference on Engineering Geophysics, Al Ain, UAE, 16–19 October 2023, Society of Exploration Geophysicists, 282–286.

James, P., and P. Ferreira, 2013, Geophysical Modeling of Typical Cavity Shapes to Calculate Detection Probability and Inform Survey Design: Journal of Environmental and Engineering Geophysics, **18**, 297–316.

Levander, A. R., and K. Holliger, 1992, Small-scale heterogeneity and large-scale velocity structure of the continental crust: Journal of Geophysical Research: Solid Earth, **97**, 8797–8804.

Miller, R. D., T. S. Anderson, J. Ivanov, J. C. Davis, R. Olea, C. Park, D. W. Steeples, M. L. Moran, and J. Xia, 2003, 3-D characterization of seismic properties at the smart weapons test range, YPG: SEG Technical Program Expanded Abstracts 2003, Society of Exploration Geophysicists, 1195–1198.

Miller, R. D., and D. W. Steeples, 1991, Detecting voids in a 0.6 m coal seam, 7 m deep, using seismic reflection: Geoexploration, **28**, 109–119.

Mochales, T., E. L. Pueyo, A. M. Casas, and M. A. Soriano, 2007, Magnetic prospection as an efficient tool for doline detection: a case study in the central Ebro Basin (northern Spain): Geological Society, London, Special Publications, **279**, 73–84.

Morton, S., S. Peterie, J. Ivanov, R. Miller, D. Feigenbaum, S. Sloan, M. Moran, and H. Cudney, 2016, Feasibility study using surface wave attenuation and seismic quality factor for tunnel detection at the Yuma Proving Ground, AZ: Presented at the SEG Technical Program Expanded Abstracts 2016, OnePetro.

Morton, S. L. C., S. L. Peterie, J. Ivanov, R. D. Miller, and S. D. Sloan, 2017, Joint interpretation of multicomponent surface-wave data for tunnel detection: SEG Technical Program Expanded Abstracts 2017, Society of Exploration Geophysicists, 5458–5464.

Nakata, N., and G. C. Beroza, 2016, Reverse time migration for microseismic sources using the geometric mean as an imaging condition: Geophysics, **81**, no. 2, KS51–KS60.

Oren, C., and J. Shragge, 2021, PS energy imaging condition for microseismic data — Part 1: Theory and applications in 3D isotropic media: Geophysics, **86**, no. 2, KS37–KS48.

Peterie, S. L., J. Ivanov, E. Knippel, R. D. Miller, and S. D. Sloan, 2021, Shallow tunnel detection using converted surface waves: Geophysics, **86**, no. 3, WA59–WA68.

Peterie, S. L., and R. D. Miller, 2015, Near-surface scattering phenomena and implications for tunnel detection: Interpretation, **3**, no. 1, SF43–SF54.

Peterie, S. L., R. D. Miller, J. Ivanov, and S. D. Sloan, 2020, Shallow tunnel detection using SH-wave diffraction imaging: Geophysics, **85**, no. 2, EN29–EN37.

Rickards, B. T., D. Steeples, R. Miller, J. Ivanov, S. Peterie, S. D. Sloan, and J. R. McKenna, 2011, Near-surface Shear-wave Velocity Measurements In Unlithified Sediment: Presented at the SEG Technical Program Expanded Abstracts 2011, OnePetro.

Rocha, D., N. Tanushev, and P. Sava, 2016, Isotropic elastic wavefield imaging using the energy norm: Geophysics, **81**, no. 4, S207–S219.

Rodríguez Castillo, R., and R. Reyes Gutiérrez, 1992, Resistivity identification of shallow mining cavities in Real del Monte, Mexico: Engineering Geology, **33**, 141–149.

Rybakov, M., V. Goldshmidt, L. Fleischer, and Y. Rotstein, 2001, Cave detection and 4-D monitoring: A microgravity case history near the Dead Sea: The Leading Edge, **20**, 896–900.

Rybakov, M., Y. Rotstein, B. Shirman, and A. Al-Zoubi, 2005, Cave detection near the Dead Sea—a micromagnetic feasibility study: The Leading Edge, **24**, 585–590.

Schwenk, J. T., 2013, Constrained Parameterization of the Multichannel Analysis of Surface Waves Approach with Application at Yuma Proving Ground, Arizona: Master's thesis, Kansas University.

Schwenk, J. T., S. D. Sloan, J. Ivanov, and R. D. Miller, 2016, Surface-wave methods for anomaly detection: Geophysics, **81**, no. 4, EN29–EN42.

Schwenk, J. T., S. D. Sloan, R. D. Miller, and J. Ivanov, 2014, Correlation of the backscatter analysis of surface waves method (BASW) for anomaly detection, *in* SEG Technical Program Expanded Abstracts 2014: Society of Exploration Geophysicists, SEG Technical Program Expanded Abstracts, 2029–2035.

Shragge, J., A. J. Girard, C. Oren, and R. Krahenbuhl, 2024, Elastic time-reverse imaging of backscattered surface-wave data: Geophysics, **89**, no. 4, KS119–KS128.

Sloan, S. D., S. L. Peterie, R. D. Miller, J. Ivanov, J. T. Schwenk, and J. R. McKenna, 2015, Detecting clandestine tunnels using near-surface seismic techniques: Geophysics, **80**, no. 5, EN127–EN135.

Smith, J. A., D. Borisov, H. Cudney, R. D. Miller, R. Modrak, M. Moran, S. L. Peterie, S. D. Sloan, J. Tromp, and Y. Wang, 2019, Tunnel detection at Yuma Proving Ground, Arizona, USA — Part 2: 3D full-waveform inversion experiments: Geophysics, **84**, no. 1, B107–B120.

Styles, P., S. Toon, E. Thomas, and M. Skittrall, 2006, Microgravity as a tool for the detection, characterization and prediction of geohazard posed by abandoned mining cavities: First Break, **24**, no. 5.

Wang, Y., R. D. Miller, S. L. Peterie, S. D. Sloan, M. L. Moran, H. H. Cudney, J. A. Smith, D. Borisov, R. Modrak, and J. Tromp, 2019, Tunnel detection at Yuma Proving Ground, Arizona, USA — Part 1: 2D full-waveform inversion experiment: Geophysics, **84**, no. 1, B95–B105.

Weiss, R. M., and J. Shragge, 2013, Solving 3D anisotropic elastic wave equations on parallel GPU devices: Geophysics, **78**, no. 2, F7–F15.

Witten, B., and J. Shragge, 2017, Image-domain velocity inversion and event location for microseismic monitoring: Geophysics, **82**, no. 5, KS71–KS83.

Xu, X., Q. Zeng, D. Li, J. Wu, X. Wu, and J. Shen, 2010, GPR detection of several common subsurface voids inside dikes and dams: Engineering Geology, **111**, 31–42.

Yuan, J., J. Yu, X. Fu, and C. Han, 2020, Antinoise performance of time-reverse imaging conditions for microseismic location: Geophysics, **85**, no. 3, KS75–KS87.